

Fluctuating charge order in the optimally doped high temperature superconductor $\text{Bi}_2\text{Sr}_2\text{CaCu}_2\text{O}_{8+x}$

Sean Vig¹, Anshul Kogar¹, Vivek Mishra², Luc Venema¹, Melinda S. Rak¹, Ali A. Husain¹, Peter D. Johnson³, Genda D. Gu³, Eduardo Fradkin¹, Michael R. Norman², Peter Abbamonte^{1,*}

¹ Department of Physics and Materials Research Laboratory, University of Illinois, Urbana, IL, 61801

² Materials Science Division, Argonne National Laboratory, Argonne, IL, 60439, USA

³ Condensed Matter Physics and Materials Science Department, Brookhaven National Laboratory, Upton, NY, 11973, USA

* Email: abbamonte@mrl.illinois.edu

The field of high temperature superconductivity has been revolutionized by the recent discovery of charge order in most families of underdoped copper-oxides [1,2,3,4,5,6]. Little is known, however, about the dynamics of this order, or whether it is present in optimally doped materials in which superconductivity is most pronounced. Here we present the first momentum-resolved, electron energy-loss (M-EELS) study of charge order in an optimally doped high temperature superconductor, $\text{Bi}_2\text{Sr}_2\text{CaCu}_2\text{O}_{8+x}$, carried out with energy resolution $\Delta E = 4.5$ meV. We observed the emergence at low temperature of diffuse, short-ranged charge order that undergoes quasielastic fluctuations on a time scale $\tau = 160$ fs. This order interacts with several bosonic collective modes whose spectral weight provides a transparent understanding of the so-called “kink” structure observed with photoemission in this material [7,8]. Our study suggests that superconductivity in the copper-oxides coexists with a dynamic, inhomogeneous state that influences the magnitude of electron-boson interactions.

The origin of high temperature superconductivity in copper-oxides continues to be one of the great unsolved problems of condensed matter physics. The landscape of the field was recently changed by the discovery, by resonant x-ray scattering (RXS), that charge order is a general feature of the underdoped phase diagram [1,2,3,4,5,6,9].

Little is known, however, about the role of charge order in optimally doped materials—away from the pseudogap regime—in which the order is believed to be short-ranged or fluctuating [10,11]. A limitation on the RXS technique is that it lacks energy resolution, integrating over all scattered photons. Consequently, nothing is known about the time scale of the observed charge order, or whether it is static or fluctuating. Moreover, RXS cannot distinguish between coherent scattering and incoherent fluorescence, the latter forming a diffuse background that is many times more intense in RXS than the charge order signal itself [1,3,4,5,6]. This background is indistinguishable from diffuse scattering characteristic of short-ranged order. So it is not known whether charge order is present in the superconducting state, or what are its temporal characteristics.

What is needed, then, is an meV-energy-resolved scattering technique sensitive to the momentum-dependent, collective charge response of the system. Such a technique could detect short-ranged or fluctuating charge order, and would also reveal the elementary, bosonic charge excitations. The latter could provide insight into the origin of the mysterious boson self-energy anomalies observed in angle-resolved photoemission (ARPES) and scanning tunneling microscopy (STM) measurements [7,8,12,13].

We developed an instrument for momentum-resolved, low-energy, electron energy-loss spectroscopy (“M-EELS” [14,15]). The instrument is based on an Ibach-type HR-EELS spectrometer [16], commonly used in surface science, which was motorized and retrofitted with a five-axis, low temperature sample goniometer equipped with the same degrees of freedom as spectrometers used for inelastic x-ray or neutron scattering (see **Methods**). This instrument achieves an energy resolution of 2.2 meV, a momentum resolution of 0.02 \AA^{-1} in the scattering plane, and can access multiple Brillouin zones. The M-EELS scattering cross section is given by

$$\frac{\partial^2 \sigma}{\partial \Omega \partial E} = \sigma_0 V_{\text{eff}}^2 (k_i^z, k_s^z, q) \cdot S(\mathbf{q}, \omega) \quad (1)$$

where $S(\mathbf{q}, \omega)$ is the charge dynamic structure factor of the surface and $\sigma_0 V_{\text{eff}}$ is the relevant Coulomb matrix element [14,16,17,18]. $S(\mathbf{q}, \omega)$ is the fundamental charge correlation function [19], revealing both static and fluctuating order as well as the bosonic charge excitations that exist at the meV scale. $S(\mathbf{q}, \omega)$ is related to the bosonic spectral function, $\chi''(\mathbf{q}, \omega)$, via the fluctuation-dissipation theorem,

$$S(\mathbf{q}, \omega) = \frac{1}{\pi} \frac{1}{e^{-\hbar\omega/k_B T} - 1} \chi''(\mathbf{q}, \omega). \quad (2)$$

This spectral function is directly related to the inverse dielectric function, and quantifies the charge susceptibility, i.e., the tendency of a material to exhibit charge order [20]. In the limit $\mathbf{q} \rightarrow 0$, it also defines the electronic compressibility of the system [19,21]. $\chi''(\mathbf{q}, \omega)$ may also serve as the boson Green’s function in electron self-energy calculations [22], potentially providing insight into the origin of self-energy features in ARPES and STM experiments.

The key advantage of M-EELS, compared to other energy-resolved scattering techniques, is that it couples to the charge density of the system. By contrast, inelastic neutron scattering (INS) is insensitive to charge excitations unless they cause displacements in the structural lattice, since a neutron is electrically neutral. Inelastic x-ray scattering (IXS) couples to the electron density, not the

charge density, so is oversensitive to lattice excitations, since most electrons reside in core states [23]. For this reason, many x-ray researchers have turned to resonant IXS (RIXS) to enhance scattering from valence band excitations. But how to relate the RIXS cross section to a spectral function is still unknown [24]. A disadvantage of M-EELS is that it is surface-sensitive. But because it measures the spectral function of interest, it can play a similar role for the bosons to that played by ARPES for the fermions.

The M-EELS energy spectrum for optimally doped Bi2212, measured at $\mathbf{q} = 0$, is shown in Fig. 1*a*. At least four collective modes are visible, at 17 meV, 24 meV, 49 meV, and 80 meV, which were observed in standard HR-EELS surface studies dating back to 1989 [25,26,27,28,29]. Fig. 1*a* reveals that these peaks reside on an energy-independent continuum that extends above 0.3 eV, which is related to the Raman continuum believed to be a signature of marginal-Fermi-liquid scaling [18,30]. We performed a complete, two-dimensional momentum map of the M-EELS spectra through a 45° sector of the Brillouin zone. The dispersion of the modes was consistent with a previous measurement carried out along high-symmetry directions [29] (Fig. 1*c-d*).

These modes have the correct energy to be the origin of the dispersion kinks observed with ARPES [7,8,22]. Their identity, however, is not settled. Early HR-EELS studies attributed them to phonons involving oxygens at the apical site and in the BiO layer [25]. However, similar modes observed with INS in $\text{HgBa}_2\text{CuO}_{4+\delta}$ (Hg1201) [31] and IXS in single-layer $\text{Bi}_2\text{Sr}_2\text{CuO}_{6+\delta}$ (Bi2201) [32] were attributed to Ising-like magnetic excitations and phonons in the CuO_2 plane, respectively. To clarify this issue, we exploit the relationship between the M-EELS cross section and the inverse dielectric function by comparing our data at $\mathbf{q}=0$ to the *c*-axis optical response of optimally doped Bi2212 measured with infrared reflectivity (IR) [33] (Fig. 1*b*). The similarity is striking considering that M-EELS measures the surface and IR is a bulk probe, and identify these modes as a spectrum of at least ten, distinct, *c*-axis-polarized optical phonons involving excitations in both the CuO_2 and BiO layers [33].

To search for valence band charge order in optimally doped Bi2212, we performed a two-dimensional momentum map of the elastic ($\omega=0$) scattering at room temperature (Fig. 2*a*). The known structural features of Bi2212 are visible, including the (1,0) Bragg peak and the (0.11, 0.11) structural supermodulation, as well as its harmonics [12,34]. These features demonstrate the momentum control of M-EELS and its ability to pinpoint charge features in momentum space.

Cooling to $T = 20\text{K}$, a pattern of diffuse scattering appears (Fig. 2*b*). The signal was found to be highly directional, forming rods along the (1,0) and (1,1) lines in momentum space, each subtending an angle of less than 20° , indicating the existence of short-ranged charge order with a high degree of angular orientation. This effect was observed in two different samples, was reversible in temperature, and exhibited no time dependence [18]. Nevertheless, to check if it could be a surface effect, we compared the elastic scattering in the (1,0) direction to that from an underdoped Bi2212 crystal with $T_C = 50\text{K}$, whose cleaved BiO surface has identical chemistry and adhesion properties for residual gases in a vacuum system (Fig. 2*c*). Under the same conditions, elastic scattering appeared at low temperature from this sample as well, but exhibited a peak at $H = 0.38\text{ r.l.u.}$, rather than diffuse scattering, indicating the existence of well-defined charge order with correlation length $\xi \sim 8a$, similar to RXS observations on underdoped cuprates [3,5]. The pronounced doping dependence indicates that the scattering in Fig. 2*a,b* is not just a surface effect, but an intrinsic property of optimally doped Bi2212.

The observed short-ranged order is not static. In Fig. 3 we compare energy cuts through one of the rods of scattering to that for the (0.11, 0.11) supermodulation reflection, which serves as a static reference. The diffuse scattering was found to be quasielastic, exhibiting relaxational dynamics on an energy scale of 26 meV. The dynamic character of this order contrasts with that in underdoped cuprates, whose associated lattice displacements have been shown by IXS to be static on energy scales below 100

μeV [35,36]. Order of this type would be invisible to truly static probes, such as STM, and supports the picture of fluctuating charge order coexisting with superconductivity near optimal doping [10].

The momentum tunability of M-EELS enables a quantitative comparison between the bosonic modes in Fig. 1 and the kink features observed with ARPES [7,8]. Using data from M-EELS, we constructed the full bosonic spectral function, $\chi''(\mathbf{q}, \omega)$, by eliminating the Coulomb matrix element in Eq. 1 and the Bose factor in Eq. 2. The former was simply divided from the data. We developed a new antisymmetrization procedure to eliminate the latter that properly handles the divergence at $\omega = 0$ ([14,18]; Fig. 1b). The resulting constant-energy slices of $\chi''(\mathbf{q}, \omega)$ are shown in Fig. 4a-l.

Fig. 4 reveals a significant enhancement in the spectral weight in the collective modes at wave vectors corresponding to both the charge order and the supermodulation features. This enhancement, which was also observed in the vicinity of spin order [37], can be understood as a double-scattering effect or, equivalently, an Umklapp process in which the probe electron acquires its momentum from the lattice rather than the excitation it creates. This spectral weight supports the picture that c -axis displacements are integrally involved in the formation of charge order [38]. Given that such displacements couple strongly to the in-plane charge density [39], one expects the presence of charge order to influence, at least indirectly, the magnitude of the electron self-energy renormalization by modes of this type [40,7,8].

Using this bosonic spectral function, we calculated the electron self-energy in a one loop approximation ($\Sigma = \int \chi G_0$) [18,21,22 ; see **Methods**]. The resulting dispersion along the (1,1) (nodal) direction is compared to ARPES data at $T = 115 \text{ K}$ ($> T_c$) in Fig. 4m. The agreement between the two curves is excellent, and provide an estimated total electron-boson coupling constant of $\lambda = 0.7$, which is in line with previous estimates [41], This one-loop calculation is simplistic but indicates that the c -axis modes we see have the right dispersion to explain the ARPES kinks [7,8].

What kind of charge order could give rise to rods of scattering (Fig. 2b)? In a perfectly ordered state, the scattering would exhibit sharp Bragg peaks at momenta defined by the periodicity of the order. If defects are introduced into the charge order, such as domain walls or dislocations, the peaks do not vanish but broaden, taking on a width inversely related to the distance between defects, the integrated intensity remaining constant as long as the local amplitude of the order is unchanged. In the limit in which the locations of the defects are completely random, the Bragg scattering broadens into a diffuse background.

What rods of scattering imply is that the charge order in optimally doped Bi2212 has a large amplitude but exhibits randomly located defects that are well-oriented, maintaining angular registry with the underlying crystal lattice. A charge ordered state with a large number of randomly positioned domain walls, constrained to run either parallel to or 45° from the CuO bond direction, would be consistent with the observed pattern. Such a phase would exhibit the same symmetries as a nematic state, the defects serving as effective “nematogens” [42]. Whatever their nature, the defects fluctuate on a time scale $\tau = 2\pi\hbar / 26 \text{ meV} = 160 \text{ fs}$, supporting the picture that optimally doped cuprates, outside of the pseudogap phase, are characterized by charge order that is fluctuating on a fast time scale [10].

Methods

M-EELS experiments were carried out at beam energies ranging from 7 to 50 eV on crystals of optimally doped Bi2212 with $T_c = 92 \text{ K}$ and an underdoped crystal with $T_c = 50 \text{ K}$, cleaved under vacuum. Elastic scattering from the

(1,0) Bragg and (0.11,0.11) supermodulation reflections were used *in situ* to construct an orientation matrix translating between diffractometer angles and reciprocal space. In this paper, ω denotes the energy transferred to the sample from the electron, and Miller indices (H, K) designate the transferred momentum in tetragonal units, i.e., $\mathbf{q} = 2\pi (H, K)/a$, where $a = 3.85 \text{ \AA}$ is the tetragonal, in-plane lattice parameter [18].

Self-energy calculations were carried out in the Lehmann representation. The bare Green's function, G_0 , was taken from tight binding fits to ARPES data [43] and adjusted to match the bare Fermi velocity at high energies. The electron-boson coupling constants were approximated as being momentum-independent, and chosen to reproduce the low energy Fermi velocity. To fill all of momentum space from the 45° octant measured, the system was assumed to have four-fold (C_4) symmetry and the data replicated to fill momentum space [18].

Acknowledgements

We gratefully acknowledge helpful input from L. H. Santos, J. M. Tranquada, C. M. Varma, and J. C. Davis. This work was supported by the Center for Emergent Superconductivity, an Energy Frontier Research Center funded by the U.S. Department of Energy, Office of Basic Energy Sciences under Award # DE-AC02-98CH10886. P.A. acknowledges support from the EPiQS program of the Gordon and Betty Moore Foundation, grant # GBMF4542. E. F. acknowledges DOE Award No. DE-SC0012368.

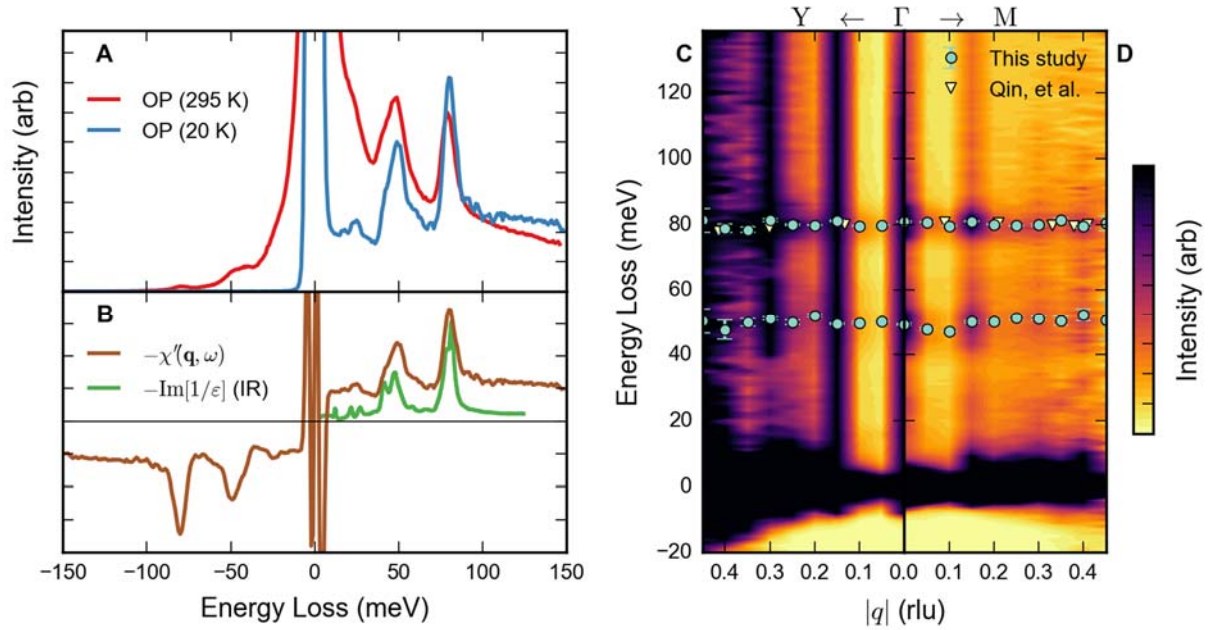


Figure 1 Bosonic excitations of optimally doped Bi2212 measured with M-EELS. (a) Excitation spectrum at $\mathbf{q}=(0,0)$ for two different temperatures, showing well-defined features at 17 meV, 24 meV, 49 meV, and 80 meV. These excitations reside on a broad, marginal Fermi liquid (MFL) continuum that extends to above 0.3 eV [18]. Apart from thermal broadening effects, no significant changes in lineshape with temperature could be discerned at this momentum. (b) Bosonic spectral function, $\chi''(\mathbf{q}, \omega)$, at $\mathbf{q}=(0,0)$ obtained by antisymmetrizing the M-EELS data [18] (brown line), compared to the inverse dielectric function measured with infrared reflectivity (IR) for *c*-axis-polarized light [33] (green line). (c) Dispersion of the excitations (circles) along the (1,1) direction compared to a previous study (triangles) carried out along high-symmetry directions [29]. The enhancement of spectral weight due to interaction with static order is clearly visible in this plot (see text). (d) Same measurements as (c), but along the (1,0) or antinodal direction.

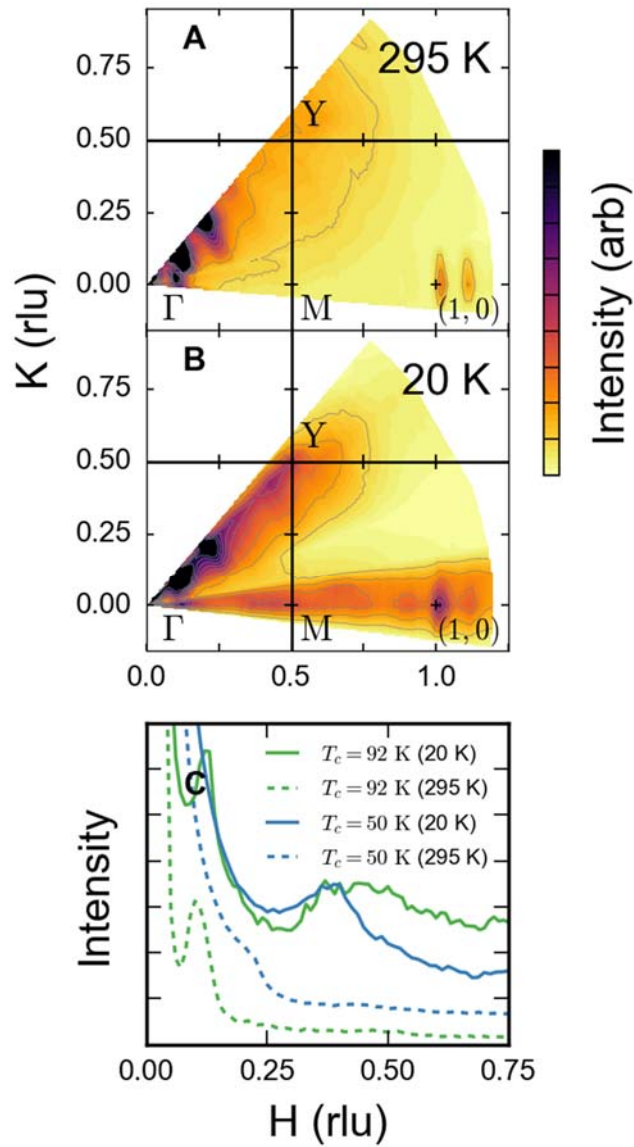


Figure 2 Emergence of short-ranged charge order at low temperature. (a) Two-dimensional reciprocal space map of the elastic ($\omega = 0$) scattering taken at $T = 295$ K at resolution $\Delta E = 4.5$ meV. The strong features along the diagonal, (1, 1) direction correspond to the structural supermodulation and its harmonics. The sharp feature near (1,0) is the Bragg reflection at the center of the second Brillouin zone [18]. (b). Same scan as (a) taken at $T = 20$ K, showing the appearance of diffuse scattering rods along the (1, 0) and (1, 1) symmetry axes. (c) Line plots of diffuse scattering along the (1, 0) direction compared to that for an underdoped crystal with $T_c = 50$ K. The strong dependence on doping suggests that this scattering is not a surface effect, but an intrinsic property of optimally doped Bi2212.

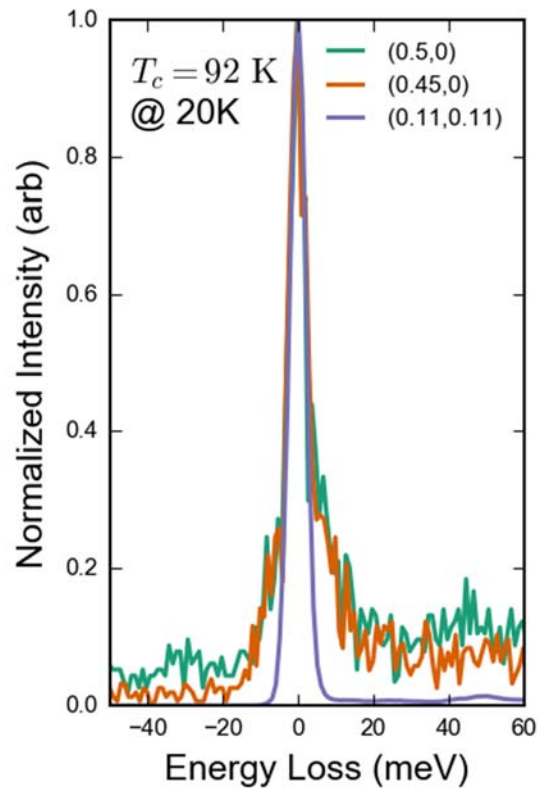


Figure 3 Dynamical nature of the short-ranged charge order in optimally-doped Bi2212. Shown are fixed-energy momentum cuts through the diffuse rod at $\mathbf{q}=(0.5, 0)$ (green line) and $\mathbf{q}=(0.45, 0)$ (orange line), and through the supermodulation reflection at $\mathbf{q}=(0.11, 0.11)$ (purple line), which serves as a static reference. The diffuse scattering exhibits quasielastic broadening of ~ 26 meV compared to the static supermodulation, indicating that the short-ranged charge order is fluctuating on a time scale $\tau \sim 400$ fs.

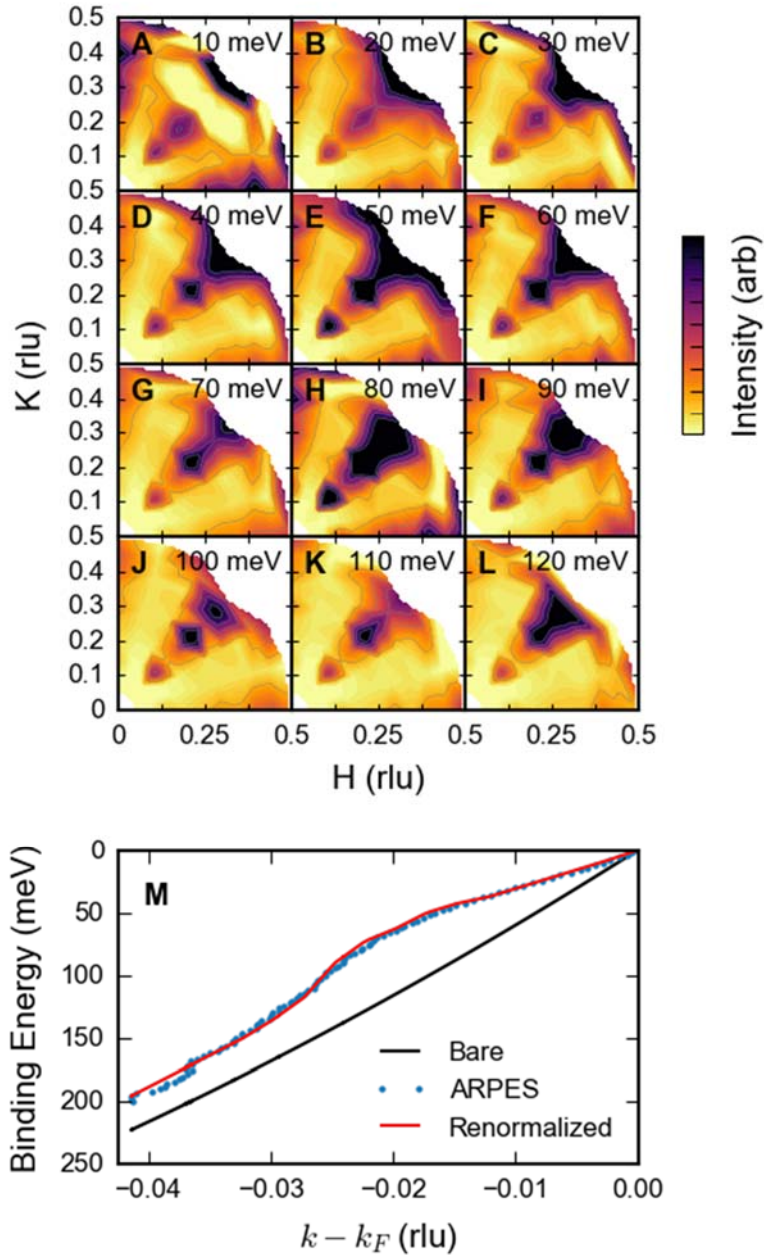


Figure 4 Bosonic spectral function of optimally doped Bi2212 and its calculated effect on ARPES dispersions. (a-l) Fixed-energy momentum cuts of $\chi''(\mathbf{q}, \omega)$ at $T = 20$ K for different values of ω . The data have been divided by q^2 to improve the visibility of features at lower momenta. Panels (e) and (h) show enhanced weight of the 49 meV and 80 meV excitations at wave vectors corresponding to the charge order and the structural supermodulation due to Umklapp effects (see text). (m) Results of a one-loop self-energy calculation, using the spectral function panels (a-l), compared with ARPES data [18], suggesting a total electron-boson coupling of $\lambda \sim 0.7$.

References

- 1 Abbamonte, P., Rusydi, A., Smadici, S., Gu, G. D., Sawatzky, G. A., Feng, D. L., Spatially modulated 'Mottness' in $\text{La}_{2-x}\text{Ba}_x\text{CuO}_4$, *Nature Phys.* **1**, 155-158 (2005)
- 2 Ghiringhelli, G., Le Tacon, M., Minola, M., Blanco-Canosa, S., Mazzoli, C., Brookes, N. B., De Luca, G. M., Frano, A., Hawthorn, D. G., He, F., Loew, T., Moretti Sala, M., Peets, D. C., Salluzzo, M., Schierle, E., Sutarto, R., Sawatzky, G. A., Weschke, E., Keimer, B., Braicovich, L., *Science* **337**, 821 (2012)
- 3 Comin, R., Frano, A., Yee, M. M., Yoshida, Y., Eisaki, H., Schierle, E., Weschke, E., Sutarto, R., He, F., Soumyanarayanan, A., He, Y., Le Tacon, M., Elfimov, I. S., Hoffmann, J. E., Sawatzky, G. A., Keimer, B., Damascelli, A., Charge order driven by fermi-arc instability in $\text{Bi}_2\text{Sr}_{2-x}\text{La}_x\text{CuO}_{6+\delta}$, *Science* **343**, 390-392 (2014)
- 4 da Silva Neto, E. H., Comin, R., Feizhou, H., Sutarto, R., Jiang, Y., Greene, R., Sawatzky, G. A., Damascelli, A., Charge ordering in the electron-doped superconductor $\text{Nd}_{2-x}\text{Ce}_x\text{CuO}_4$, *Science* **347**, 282-285 (2015)
- 5 Da Silva Neto, E. H., Aynajian, P., Frano, A., Comin, R., Schierle, E., Weschke, E., Gyenis, A., Wen, J., Schneeloch, J., Xu, Z., Ono, S., Gu, S., Le Tacon, M., Yazdani, A., Ubiquitous Interplay Between Charge Ordering and High Temperature Superconductivity in Cuprates, *Science* **343**, 393 (2014)
- 6 Tabis, W., Li, Y., Le Tacon, M., Braicovich, L., Kreyssig, A., Minola, M., Dellea, G., Weschke, E., Veit, M. J., Ramazanoglu, M., Goldman, A. I., Schmitt, T., Ghiringhelli, G., Barisic, N., Chan, M. K., Dorow, C. J., Yu, G., Zhao, X., Keimer, B., Greven, M., Charge order and its connection with Fermi-liquid charge transport in a pristine high- T_c cuprate, *Nature Comm.* **5**, 5875 (2014)
- 7 Vishik, I. M., Lee, W. S., He, R.-H., Hashimoto, M., Hussain, Z., Devereaux, T. P., Shen, Z. X., ARPES studies of cuprate Fermiology: superconductivity, pseudogap, and quasiparticle dynamics, *New J. Phys.* **12**, 105008 (2010)
- 8 Cuk, T., Lu, D. H., Zhou, X. J., Shen, Z. X., Devereaux, T. P., Nagaosa, N., A review of electron-phonon coupling seen in the high- T_c superconductors by angle-resolved photoemission studies (ARPES), *Phys. Stat. Sol. (b)* **242**, 11-29 (2005)
- 9 Keimer, B., Kivelson, S. A., Norman, M. R., Uchida, S., Zaanen, J., From quantum matter to high-temperature superconductivity in copper oxides, *Nature* **518**, 179-186 (2015)
- 10 Kivelson, S. A., Bindloss, I. P., Fradkin, E., Oganessian, V., Tranquada, J. M., Kapitulnik, A., Howald, C., How to detect fluctuating stripes in the high-temperature superconductors, *Rev. Mod. Phys.* **75**, 1201-1241 (2003)
- 11 Hanaguri, T., Lupien, C., Kohsaka, Y., Lee, D.-H., Azuma, M., Takano, M., Takagi, H., Davis, J. C., A 'checkerboard' electronic crystal state in lightly hole-doped $\text{Ca}_{2-x}\text{Na}_x\text{CuO}_2\text{Cl}_2$, *Nature* **430**, 1001-1005 (2004)
- 12 J. Lee, K. Fujita, K. McElroy, J. A. Slezak, M. Wang, Y. Aiura, H. Bando, M. Ishikado, T. Masui, J.-X. Zhu, A. V. Balatsky, H. Eisaki, S. Uchida, J. C. Davis, Interplay of electron-lattice interactions and superconductivity in $\text{Bi}_2\text{Sr}_2\text{CaCu}_2\text{O}_{8+\delta}$, *Nature* **442**, 546-550 (2006)
- 13 Fujita, K., Schmidt, A. R., Kim, E.-A., Lawler, M. J., Lee, D. H., Davis, J. C., Eisaki, H., Uchida, S., Spectroscopic Imaging Scanning Tunneling Microscopy Studies of Electronic Structure in the Superconducting and Pseudogap Phases of Cuprate High- T_c Superconductors, *J. Phys. Soc. Jpn.* **81**, 011005 (2012)
- 14 Kogar, A., Vig, S., Gan, Y., Abbamonte, P., Temperature-resolution anomalies in the reconstruction of time dynamics from energy-loss experiments, *J. Phys. B: At. Mol. Opt. Phys.* **4**, 124034 (2014)
- 15 Kogar, A., Vig, S., Thaler, A., Wong, M. H., Xiao, Y., Reig-i-Plessis, D., Cho, G. Y., Valla, T., Pan, Z., Scheenloch, J., Zhong, R., Gu, G. D., Hughes, T. L., MacDougall, G. J., Chiang, T.-C., Abbamonte, P.,

-
- Surface Collective Modes in the Topological Insulators Bi_2Se_3 and $\text{Bi}_{0.5}\text{Sb}_{1.5}\text{Te}_{3-x}\text{Se}_x$, *Phys. Rev. Lett.* **115**, 257402 (2015)
- 16 Ibach, H., Mills, D. L., *Electron Energy Loss Spectroscopy and Surface Vibrations*. New York, NY: Academic Press, 1982
 - 17 Mills, D. L., The scattering of low energy electrons by electric field fluctuations near crystal surfaces, *Surface Science* **48**, 59-79 (1975)
 - 18 *Supplementary information is available in the online version of the paper.*
 - 19 Pines, D., Nozieres, P., *Theory of Quantum Liquids*. New York, NY: Perseus, 1999
 - 20 Grüner, G., *Density Waves in Solids*. Cambridge, MA: Perseus, 1994
 - 21 Mahan, G. D., *Many-Particle Physics*. New York, NY: Kluwer Academic/Plenum, 2000
 - 22 Devereaux, T. P., Cuk, T., Shen, Z. X., Nagaosa, N., Anisotropic electron-phonon interaction in the cuprates, *Phys. Rev. Lett.* **93**, 117004 (2004)
 - 23 Schülke, W., *Electron Dynamics by Inelastic X-Ray Scattering*. Oxford, U.K.: Oxford University Press, 2007
 - 24 See, for example, Benjamin, D., Klich, I., Demler, E., Single-Band Model of Resonant Inelastic X-Ray Scattering by Quasiparticles in High-Tc Cuprate Superconductors, *Phys. Rev. Lett.* **112**, 247002 (2014)
 - 25 Phelps, R. B., Akavoor, P., Kesmodel, L. L., Demuth, J. E., Mitzi, D. B., Surface phonons on $\text{Bi}_2\text{Sr}_2\text{CaCu}_2\text{O}_{8+x}$, *Phys. Rev. B* **48**, 12936-12940 (1993)
 - 26 Persson, B. N. J., Demuth, J. E., High-resolution electron-energy-loss study of the surfaces and energy gaps of cleaved high-temperature superconductors, *Phys. Rev. B* **42**, 8057-8072 (1990)
 - 27 Li, H., Lieber, C. M., The energy gap in the high-Tc copper-oxide superconductors, *Mod. Phys. Lett. B* **7**, 143-153 (1993)
 - 28 Demuth, J. E., Persson, B. N. J., Holtzberg, F., Chandrasekhar, C. V., Surface and superconducting properties of cleaved high-temperature superconductors, *Phys. Rev. Lett.* **64**, 603-606 (1990)
 - 29 Qin, H., Shi, J., Cao, Y., Wu, K., Zhang, J., Plummer, E. W., Wen, J., Xu, Z. J., Gu, G. D., Guo, J., Direct determination of the electron-phonon coupling matrix element in a correlated system, *Phys. Rev. Lett.* **105**, 256402 (2010)
 - 30 Varma, C. M., Littlewood, P. B., Schmitt-Rink, S., Abrahams, E., Ruckenstein, A. E., Phenomenology of the normal state of Cu-O high temperature superconductors, *Phys. Rev. Lett.* **18**, 1996-1999 (1989)
 - 31 Li, Y., Yu, G., Chan, M. K., Baledent, V., Li, Y., Barisic, N., Zhao, X., Hradil, K., Mole, R. A., Sidis, Y., Steffens, P., Bourges, P., Greven, M., Two Ising-like magnetic excitations in a single-layer cuprate superconductor, *Nature Phys.* **8**, 404-410 (2012)
 - 32 Graf, J., d'Astuto, M., Jozwiak, C., Garcia, D. R., Saini, N. L., Krisch, M., Ikeuchi, K., Baron, A. Q. R., Eisaki, H., Lanzara, A., Bond Stretching Phonon Softening and Kinks in the Angle-Resolved Photoemission Spectra of Optimally Doped $\text{Bi}_2\text{Sr}_{1.6}\text{La}_{0.4}\text{Cu}_2\text{O}_6$ Superconductors, *Phys. Rev. Lett.* **100**, 227002 (2008)
 - 33 Tu, J. J., Homes, C. C., Gu, G. D., Strongin, M., A systematic optical study of phonon properties in optimally doped $\text{Bi}_2\text{Sr}_2\text{CaCu}_2\text{O}_{8+x}$ single crystals, *Physica B* **316-317**, 324-327 (2002)
 - 34 Gao, Y., Lee, P., Coppens, P., Subramanian, M. A., Sleight, A. W., The incommensurate modulation of the 2212 Bi-Sr-Ca-Cu-O superconductor, *Science* **241**, 954-956 (1998)
 - 35 Le Tacon, M., Bosak, A., Souliou, S. M., Dellea, G., Loew, T., Heid, R., Bohnen, K.-P., Ghirnigelli, G., Krisch, M., Keimer, B., Inelastic X-ray scattering in $\text{YBa}_2\text{Cu}_3\text{O}_{6.6}$ reveals giant phonon anomalies and elastic central peak due to charge-density-wave formation, *Nature Phys.* **10**, 52-58 (2014)
 - 36 Blackburn, E., Chang, J., Said, A. H., Leu, B. M., Liang, R., Bonn, D., Hardy, W. N., Forgan, E. M., Hayden, S. M., Inelastic x-ray study of phonon broadening and charge-density wave formation in ortho-II-ordered $\text{YBa}_2\text{Cu}_3\text{O}_{6.54}$, *Phys. Rev. B* **88**, 054506 (2013)

-
- 37 Wagman, J. J., Carlo, J. P., Gaudet, J., Van Gastel, G., Abernathy, D., Stone, M. B., Granroth, G. E., Kolesnikov, A. I., Savici, A. T., Kim, Y. J., Zhang, H., Ellis, D., Zhao, Y., Clark, L., Kallin, A. B., Mazurek, E., Dabkowska, H. A., Gaulin, B. D., Neutron scattering studies of spin-phonon hybridization and superconducting spin gaps in the high-temperature superconductor $\text{La}_{2-x}(\text{Sr,Ba})_x\text{CuO}_4$, *Phys. Rev. B* **93**, 094416 (2016)
 - 38 Forgan, E. M., Blackburn, E., Holmes, A. T., Briffa, A. K. R., Chang, J., Bouchenoire, L., Brown, S. D., Liang, R., Bonn, D., Hardy, W. N., Christensen, N. B., v. Zimmermann, M., Hucker, M., Hayden, S. M., *Nature Comm.* **6**, 10064 (2015)
 - 39 Bozin, E. S., Huq, A., Shen, B., Claus, H., Kwok, W. K., Tranquada, J. M., Charge-screening role of c-axis atomic displacements in $\text{YBa}_2\text{Cu}_3\text{O}_{6+x}$ and related superconductors, *Phys. Rev. B* **93**, 054523 (2016)
 - 40 Raichle, M., Reznik, D., Lamago, D., Heid, R., Li, Y., Bakr, M., Ulrich, C., Hinkov, V., Hradil, K., Lin, C. T., Keimer, B., Highly Anisotropic Anomaly in the Dispersion of the Copper-Oxygen Bond-Bending Phonon in Superconducting $\text{YBa}_2\text{Cu}_3\text{O}_7$ from Inelastic Neutron Scattering, *Phys. Rev. Lett.* **107**, 177004 (2011)
 - 41 Johnson, P. D., Fedorov, A. V., Valla, T., Photoemission studies of self-energy effects in cuprate superconductors, *J. Elect. Spect. Rel. Phen.* **117-118**, 153-164 (2001)
 - 42 Kivelson, A. S., Fradkin, E., Emery, V. J., Electronic liquid-crystal phases of a doped Mott insulator, *Nature* **393**, 550-553 (1998)
 - 43 Kaminski, A., Randeria, M., Campuzano, J. C., Norman, M. R., Fretwell, H., Mesot, J., Sato, T., Takahashi, T., Kadowaki, K., Renormalization of Spectral Line Shape and Dispersion below T_c in $\text{Bi}_2\text{Sr}_2\text{CaCu}_2\text{O}_{8+\delta}$, *Phys. Rev. Lett.* **86**, 1070 (2001)

Supplementary information for

**Fluctuating charge order in the optimally doped high temperature
superconductor $\text{Bi}_2\text{Sr}_2\text{CaCu}_2\text{O}_{8+x}$**

Sean Vig¹, Anshul Kogar¹, Vivek Mishra², Luc Venema¹, Melinda S. Rak¹, Ali A. Husain¹, Peter D. Johnson³,
Genda D. Gu³, Eduardo Fradkin¹, Michael R. Norman², Peter Abbamonte^{1,*}

¹ Department of Physics and Materials Research Laboratory, University of Illinois, Urbana, IL, 61801

² Materials Science Division, Argonne National Laboratory, Argonne, IL, 60439, USA

³ Condensed Matter Physics and Materials Science Department, Brookhaven National Laboratory,
Upton, NY, 11973, USA

* Email: abbamonte@mrl.illinois.edu

Contents:

- 1. Description of the M-EELS Cross Section (Eq. 1)**
- 2. Marginal Fermi Liquid Continuum**
- 3. Data Normalization**
- 4. Reproducibility of Charge Order Scattering**
- 5. Temperature Reversibility**
- 6. Computation of $\chi''(\mathbf{q},\omega)$ from the Scattered Intensity**
- 7. Details of Self-Energy Calculation**

1. Description of the M-EELS Cross Section (Eq. 1)

Ref. [14] provides a detailed derivation of the scattering cross section for low-energy M-EELS measurements. The treatment makes use of the distorted wave Born approximation theory developed by D. A. Mills for treating the multiple scattering problem [17]. The result presented in Ref. [14] is

$$\frac{\partial^2 \sigma}{\partial \Omega \partial E} = \sigma_0 \left[V_{\text{eff}}(k_i^z, k_s^z, q) \right]^2 \int_{-\infty}^0 dz_1 dz_2 e^{q(z_1+z_2)} S(\mathbf{q}, z_1; \mathbf{q}, z_2; \omega) \quad (S1)$$

In this expression, $S(\mathbf{q}, z_1; \mathbf{q}, z_2)$ is the three-dimensional dynamic structure factor of a semi-infinite system that is homogeneous parallel to the surface, \mathbf{q} being the in-plane component of the momentum transfer, and the quantities z_1 and z_2 describing the depth below the surface (we have taken the material to fill the half-space $z < 0$). The Coulomb matrix element

$$V_{\text{eff}}(k_i^z, k_s^z, q) = \frac{4\pi e^2}{(k_i^z + k_s^z)^2 + q^2} \quad (S2)$$

describes the coupling of the probe electron to the system, q being the magnitude of \mathbf{q} . The quantities k_i^z and k_s^z represent the perpendicular momentum components of the incident and scattered electron, respectively. In an M-EELS experiment, these two quantities normally have opposite signs, and sum approximately to zero for measurements at low energy loss in near-specular geometry. The proportionality constant

$$\sigma_0 = \sqrt{\frac{E_f}{E_i}} \frac{m}{2\pi^2 \hbar^4} \frac{|R|^2}{(1+|R|^2)^2}, \quad (S3)$$

where E_i and E_f represent the kinetic energy of the incident and scattered electron, respectively, and R is the electron reflectivity off the surface.

To arrive at Eq. 1 of the manuscript we recognize that

$$S(\mathbf{q}, \omega) = \int_{-\infty}^0 dz_1 dz_2 e^{q(z_1+z_2)} S(\mathbf{q}, z_1; \mathbf{q}, z_2; \omega) \quad (S4)$$

is the two-dimensional dynamic structure factor of the surface. This quantity is integrated over a depth $1/q$, indicating that the probe depth of M-EELS is geometry-dependent and given by the inverse of the magnitude of the in-plane momentum transfer—typically a few nm for measurements presented in this study.

The validity of Mills's theory hinges on the assumption that multiple scattering effects, which are significant in EELS, take place mainly in the elastic channel, i.e., the electron undergoes (on average) many elastic scattering events but only one inelastic event before arriving at the detector, which validates the distorted-wave approach. We expect this assumption to be valid in the range of momenta investigated in this study.

2. Marginal Fermi Liquid Continuum

The boson features described in the main manuscript lie on top of a broad, featureless, nearly energy-independent continuum that has been associated with marginal Fermi liquid scaling [30].

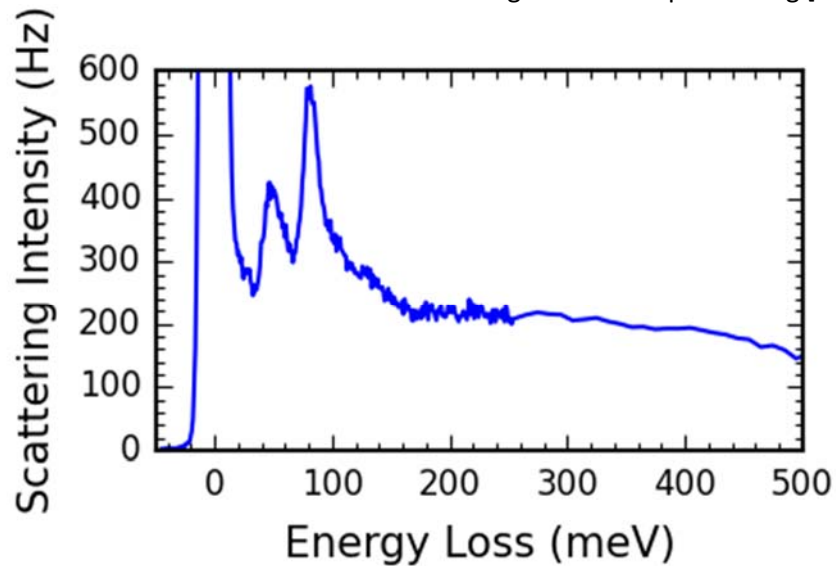


Figure S1 Wide-range M-EELS scan taken at $\mathbf{q}=0$ on optimally doped Bi2212 a showing constant, energy-independent continuum that extends beyond 0.3 eV. This continuum was also observed in early Raman scattering experiments on cuprates [S1] and was a motivation for the marginal Fermi-liquid (MFL) theory [30].

3. Data Normalization

Low-energy EELS measurements are prone to intensity drifts in time, both because of instabilities innate to the electron optics and also because of degradation of the sample surface. Proper normalization of the data is therefore critical to achieving reliable and reproducible results.

The data shown in Figs. 2 of the manuscript were taken from elastic ($\Delta E = 4.5$ meV) M-EELS scans of momentum space performed by taking radial cuts through the Γ point outward in momentum space. These data were taken with a 50 eV incident beam energy, which provides access to a large range of momentum. Purely elastic scans are relatively fast, with each radial scan taking around 20 minutes, so the sample does not degrade significantly over the duration of the scan. However, significant time elapsed between these cuts, which were sometimes performed on different cleaves. Hence, for the case of elastic scattering, normalization requires scaling the relative intensity of each of these cuts.

Because of the relatively large beam divergence perpendicular to the scattering plane, the momentum resolution perpendicular to the scan direction, $\sim 0.10 \text{ \AA}^{-1}$, is large enough for a peak from the supermodulation to be seen in each of the scans, even in the vicinity of the (1,0) direction. We therefore used this supermodulation, which is a well-characterized property of the Bi2212 structure, to scale the data at different azimuthal angles. The momentum resolution was modeled as a double Gaussian—one in the scattering plane and the other perpendicular to the scattering plane, forming a resolution

ellipsoid. Along each cut through momentum space, the supermodulation peaks were fit to a Gaussian and normalized such that their amplitudes match the resolution ellipsoid evaluated at that point.

Inelastic measurements are more time consuming. For the inelastic M-EELS measurements shown in Figs 1 and 4, a full radial cut at high energy resolution takes up to 24 hours and the full momentum space mapping involves multiple cleaves. Extensive studies showed that the initial effect of surface degradation is not a distortion of the spectra, but simply a reduction in the overall intensity, which falls off as roughly as an exponential in time, with a time constant of typically 3-5 hours at cryogenic temperatures. To correct for this decay, the elastic component of each of the inelastic scans was extracted and compared to the elastic scans, which have been corrected using the normalization scheme described above. The inelastic data were then normalized with an exponential that fit the elastic component to the normalized purely elastic scans.

At low momentum, where the radial scans have the highest point density, we clearly see both the supermodulation along the (1,1) direction and its projection onto the (1,0) direction as a result of the finite momentum resolution of the spectrometer. It is expected that the supermodulation peaks appear in this same orientation with respect to each of the Bragg peaks. In Fig. 2 it appears, however, that the satellites of the (1,0) Bragg peak are oriented along the (1,0) direction. This effect is an artifact of the low sampling density at high q values. Because of the low point density of the radial scans at high momentum, not enough points were obtained around the (1,0) Bragg peak to ascertain the precise location of the supermodulation peaks themselves.

4. Reproducibility of Charge Order Scattering

The observation of charge order presented in the main manuscript was reproduced in a second run under similar conditions on a sample from a different growth batch, as shown in Fig. S2.

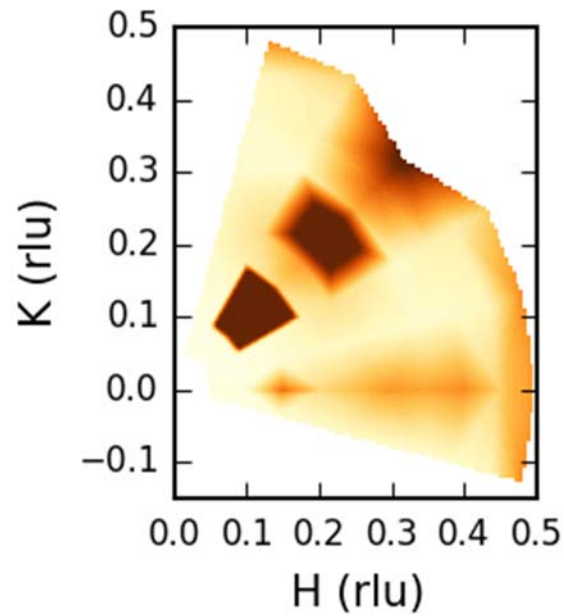


Figure S2 The static structure factor $S(\mathbf{q}, \omega=0)$ at $T = 20$ K, determined at low resolution, showing similar charge order features as in Fig. 2 of the main manuscript. Data taken from $(1,0)$ to $(1,1)$ has been folded assuming C_4 symmetry to show a 90° wedge.

5. Temperature Reversibility

The emergence of charge order was observed to be reversible in temperature, as illustrated in Fig. S3. This establishes it as a real effect, and not an artifact of surface degradation.

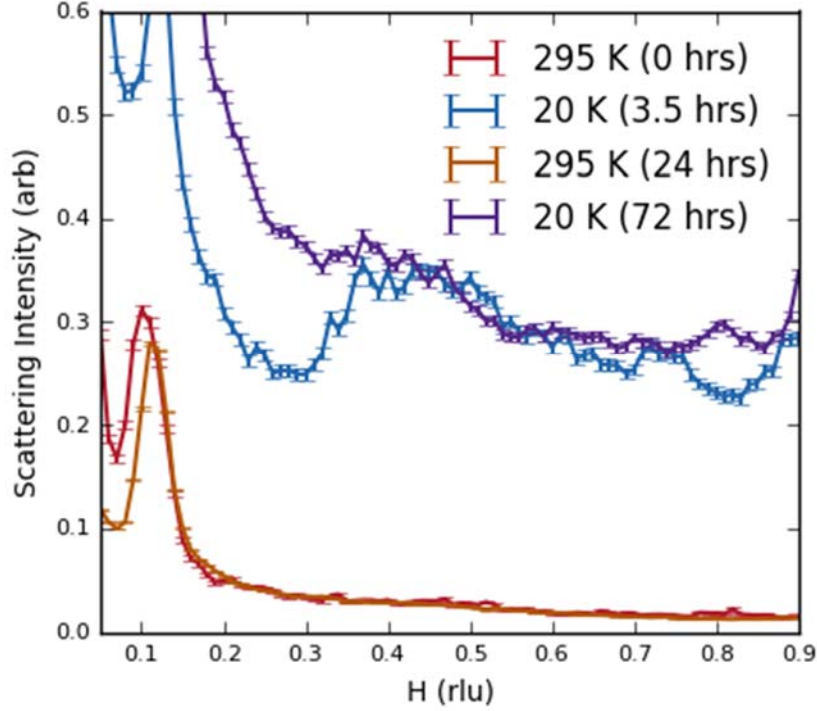


Figure S3 Time dependence of the (1,0) elastic scans on optimally doped Bi2212 showing the reversible appearance of the diffuse scattering rod at 20 K, as seen in Fig. 2 in the main paper. Note that after 72 hours, the sample surface has degraded significantly, however the rod of scattering can still be seen.

6. Computation of $\chi''(\mathbf{q}, \omega)$ from the Scattered Intensity

From the main paper Equations 1 and 2, we can write the expression for the scattering intensity measured by M-EELS, $I(\mathbf{q}, \omega)$, in terms of the dynamic susceptibility, $\chi''(\mathbf{q}, \omega)$, as:

$$I(\mathbf{q}, \omega) = -\frac{1}{\pi} \frac{\sigma_0}{1 - e^{-\beta\hbar\omega}} V_{\text{eff}}^2 \chi''(\mathbf{q}, \omega) \quad (\text{S5})$$

To extract the value of $\chi''(\mathbf{q}, \omega)$ from the measured intensity, simply dividing by the Coulomb propagator and Bose factor give reasonable values for finite momentum and energy loss, but the Bose factor diverges at $\omega=0$ and, because of finite energy resolution effects, dividing out the Bose factor introduces low energy anomalies [14]. However, if both the energy loss and energy gain scattering are measured, we can write

$$I(\mathbf{q}, \omega) - I(\mathbf{q}, -\omega) = -\frac{1}{\pi} \sigma_0 V_{\text{eff}}^2 \left[\frac{1}{1 - e^{-\beta\hbar\omega}} \chi''(\mathbf{q}, \omega) - \frac{1}{1 - e^{\beta\hbar\omega}} \chi''(\mathbf{q}, -\omega) \right] \quad (\text{S6})$$

The dynamic susceptibility is a causal propagator for the charge density, and as such satisfies the Kramers-Kronig relations, which requires the imaginary part of the electronic susceptibility to be antisymmetric, that is

$$\chi''(\mathbf{q}, \omega) = -\chi''(\mathbf{q}, -\omega) \quad (\text{S7})$$

where we have assumed the system has inversion symmetry. Using Eq. S7, we can write Eq. S6 as

$$I(\mathbf{q}, \omega) - I(\mathbf{q}, -\omega) = -\frac{1}{\pi} \sigma_0 V_{\text{eff}}^2 \chi''(\mathbf{q}, \omega) \left[\frac{1}{1 - e^{-\beta \hbar \omega}} + \frac{1}{1 - e^{\beta \hbar \omega}} \right] \quad (\text{S8})$$

$$= -\frac{1}{\pi} \sigma_0 V_{\text{eff}}^2 \chi''(\mathbf{q}, \omega) \quad (\text{S9})$$

Hence, by using the antisymmetric properties of the propagator, we can eliminate the divergence as $\omega \rightarrow 0$ while maintaining $\chi''(\mathbf{q}, \omega=0) = 0$. This antisymmetrization is analogous to the symmetrization of ARPES spectra at the Fermi momentum used to obtain the single particle spectral function, $A(\mathbf{k}, \omega)$ [S2].

In order to acquire a full, two-dimensional parameterization of $\chi''(\mathbf{q}, \omega)$, momentum scans were taken in a 45° sector from (1,0) to (1,1) (Fig. 4). In order to perform the self-energy calculation presented in the main paper, the data were folded over the full Brillouin zone assuming four-fold C_4 crystal symmetry.

7. Details of Self-Energy Calculation

The lowest order fermion self-energy is a convolution of the bare fermion Green's function, G_0 , and the interaction mediated by bosons with propagator, D , which reads

$$\Sigma(i\omega, \mathbf{k}) = g_{bf}^2 T \sum_{\Omega} \int_{\mathbf{q}} G_0(i\omega - i\Omega, \mathbf{k} - \mathbf{q}) \mathcal{D}(i\Omega, \mathbf{q}) \quad (\text{S10})$$

Here T is the temperature and g_{bf} is the boson-fermion coupling constant. The variables \mathbf{k} and \mathbf{q} are the momenta, and ω and Ω are Matsubara frequencies for the fermions and bosons, respectively. Summation over the Matsubara frequencies can be done using the spectral representation for the fermionic and bosonic Green's functions,

$$G_0(i\omega, \mathbf{k}) = \int_{-\infty}^{\infty} \frac{dy}{\pi} \frac{G_0''(y, \mathbf{k})}{y - i\omega} \quad (\text{S11})$$

$$\mathcal{D}(i\Omega, \mathbf{q}) = \int_{-\infty}^{\infty} \frac{dx}{\pi} \frac{\mathcal{D}''(x, \mathbf{q})}{x - i\Omega}$$

After performing the Matsubara summation, we analytically continue to the real frequencies. The real frequency self-energy is

$$\Sigma(i\omega \rightarrow \omega + i0^+, \mathbf{k}) = -g_{bf}^2 \int_{\mathbf{q}} \int_{-\infty}^{\infty} \frac{dx}{\pi} \chi''(x, \mathbf{q}) \left[\frac{n(x) + f(-\xi_{\mathbf{k}-\mathbf{q}})}{x + \xi_{\mathbf{k}-\mathbf{q}} - \omega - i0^+} \right] \quad (\text{S12})$$

where n and f are the Bose and the Fermi functions, respectively. Here we have used

$$G''(y, \mathbf{k} - \mathbf{q}) = -\pi \delta(y - \xi_{\mathbf{k}-\mathbf{q}}) \quad (\text{S13})$$

which is the imaginary part of the bare Green's function with a bare fermion dispersion, $\xi_{\mathbf{k}}$. For the fermions we use a tight binding dispersion, which fits the ARPES-determined Fermi surface for optimally doped Bi2212 [S3].

The fit in Ref. S3 applies to low energy ARPES data. ARPES does not measure the non-interacting dispersion, so we elected to rescale the dispersion to match the high energy ARPES data along the nodal direction, which we assume corresponds to the bare fermionic dispersion. This procedure gives a bare

nodal Fermi velocity of 2.7 eV-Å. From a numerical viewpoint, we first calculate the imaginary part of the fermion self-energy, which is,

$$\Sigma''(\omega, \mathbf{k}) = -g_{bf}^2 \sum_{\mathbf{q}} \chi''(\omega - \xi_{\mathbf{k}-\mathbf{q}}, \mathbf{q}) \left[n(\omega - \xi_{\mathbf{k}-\mathbf{q}}) + f(-\xi_{\mathbf{k}-\mathbf{q}}) \right] \quad (\text{S14})$$

The real part of the fermion self-energy is then calculated using the Kramers-Kronig relation,

$$\Sigma'(\omega, \mathbf{k}) = \frac{1}{\pi} \mathcal{P} \int_{-\infty}^{\infty} d\omega' \frac{\Sigma''(\omega', \mathbf{k})}{\omega' - \omega} \quad (\text{S15})$$

For the bosonic spectral function, we use the data from EELS measurements. Because the data consist of two main peaks, at 49 meV and 80 meV, over most of momentum space, for the purposes of the calculation we parameterized the data with the following function:

$$\chi''(\omega, \mathbf{k}) = \frac{I_1(\mathbf{k})}{V_{eff}^2(\mathbf{k})} \left[\frac{\Gamma_1^2(\mathbf{k})}{\Gamma_1^2(\mathbf{k}) + (\omega - \omega_1(\mathbf{k}))^2} - \frac{\Gamma_1^2(\mathbf{k})}{\Gamma_1^2(\mathbf{k}) + (\omega + \omega_1(\mathbf{k}))^2} \right] + \frac{I_2(\mathbf{k})}{V_{eff}^2(\mathbf{k})} \left[\frac{\Gamma_2^2(\mathbf{k})}{\Gamma_2^2(\mathbf{k}) + (\omega - \omega_2(\mathbf{k}))^2} - \frac{\Gamma_2^2(\mathbf{k})}{\Gamma_2^2(\mathbf{k}) + (\omega + \omega_2(\mathbf{k}))^2} \right] \quad (\text{S16})$$

This form fits the energy dependence of the bosonic spectral weight for the values given in Table S1. We use two effective boson-fermion coupling constants $g_{bf1/2}$ —one for each mode—as fitting parameters to match the ARPES dispersion along the nodal direction. The experimental lineshapes also have a background of the form $+b\omega^{-1}$ from the tail of the elastic line and the MFL background, which cannot provide sharp kink features so was subtracted before fitting. We find that both the 49 meV and 80 meV modes are nondispersive to a very good approximation. The momentum dependence of their intensities $(I_{1/2})/V_{eff}^2$ fits a quadratic form $p_0 + p_1 q^2$ for any given direction of q . For the 49 meV mode, the coefficients p_0 and p_1 are 7.4 and 0.10 eV⁻¹, respectively. Similarly, for 80 meV mode p_0 and p_1 are 14.6 and -0.3 eV⁻¹. The momentum dependence of the linewidths $\Gamma_{1/2}$ can be fit with a simple tight binding form,

$$\Gamma_{1/2} = \sum_{i=0}^{i=5} T_{1/2i} f_i \quad (\text{S17})$$

which produces best fit coupling constants of $g_{bf}^1 = 0.5$ eV and $g_{bf}^2 = 0.5$ eV for the 49 meV and 80 meV modes, respectively, resulting in a total electron-boson coupling, defined by $v_F / v_F^0 = (1 + \lambda)^{-1}$, of $\lambda = 0.7$. The result of this procedure is displayed in Fig. 4m of the main text.

i	f_i	T_{1i} (meV)	T_{2i} (meV)
0	1	6.96	7.44
1	$\cos k_x + \cos k_y$	-1.37	-2.86
2	$\cos k_x \cos k_y$	6.76	2.46
3	$\cos 2k_x + \cos 2k_y$	2.07	0.64
4	$\cos 2k_x \cos k_y + \cos k_x \cos 2k_y$	-4.71	-1.52

5	$\cos 2k_x \cos 2k_y$	-0.22	1.73
---	-----------------------	-------	------

Table S1 Summary of the fitting parameters used in Eqs. S16 and S17

References

[S1] D. Reznik, S. L. Cooper, M. V. Klein, W. C. Lee, D. M. Ginsberg, A. A. Maksimov, A. V. Puchkov, I. I. Tartakovskii, S.-W. Cheong, Plane-polarized Raman continuum in the insulating and superconducting layered cuprates, *Phys. Rev. B* **48**, 7624 (1993)

[S2] M. R. Norman, H. Ding, M. Randeria, J. C. Campuzano, T. Yokoya, T. Takeuchi, T. Takahashi, T. Mochiku, K. Kadowaki, P. Guptasarma, D. G. Hinks, Destruction of the Fermi surface in underdoped high- T_c superconductors, *Nature* **392**, 157 (1998)

[S3] M. R. Norman, Linear response theory and the universal nature of the magnetic excitation spectrum of the cuprates, *Phys. Rev. B* **75**, 184514 (2007) [Note: We used the dispersion tb_2 from this paper.]